Revision 1

Raman scattering and Cr^{3+} luminescence study on the structural behavior of δ-AlOOH at high pressures

Baoyun Wang[1,2], Dayong Tan[3,4], Wansheng Xiao[3,4], Xing Ding[1,4], Li Li[1,4] and Maoshuang Song[1,4*]

[1]State Key Laboratory of Isotope Geochemistry, Guangzhou Institute of Geochemistry, Chinese Academy of Sciences, Guangzhou 510640, China;

[2]College of Earth and Planetary Sciences, University of Chinese Academy of Sciences, Beijing, 100049, China;

[3]Key Laboratory of Mineralogy and Metallogeny, Guangzhou Institute of Geochemistry, Chinese Academy of Sciences, Guangzhou 510640, China;

[4]CAS Center for Excellence in Deep Earth Science, Guangzhou, 510640, China

[*]Corresponding author: M. Song (msong@gig.ac.cn)

Abstract

δ-AlOOH is regarded as a potential water carrier that is stable in the Earth's lower mantle down to the core-mantle boundary along the cold slab geotherm; thus, knowledge of its structural evolution under high pressure is very important for understanding water circulation in the Earth's interior. In this work, we conducted Raman scattering and luminescence spectroscopic experiments on δ-AlOOH at high

pressures up to 34.6 GPa and 22.1 GPa, respectively. From the collected Raman spectra, significant changes in the pressure dependence of the frequencies of Raman-active modes were observed at ~8 GPa with several modes displaying softening behaviors. In particular, the soft A_1 mode, which corresponds to a lattice vibration of the AlO_6 octahedron correlated to OH stretching vibration, decreases rapidly with increasing pressure and shows a trend of approaching 0 cm^{-1} at ~9 GPa according to a quadratic polynomial extrapolation. These results provide clear Raman-scattering spectroscopic evidence for the $P2_1nm$-to-$Pnnm$ structural transition. Similarly, the phase transition was also observed in the luminescence spectra of Cr^{3+} in both powder and single-crystal δ-AlOOH samples, characterized by abrupt changes in the pressure dependences of the wavelength of the R-lines and sidebands across the $P2_1nm$-to-$Pnnm$ transition. The continuous decrease in R_2-R_1 splitting with pressure indicated that the distortion of the AlO_6 octahedron was suppressed under compression. No abnormal features were clearly observed in our Raman or luminescence spectra at ~18 GPa, where the ordered symmetrization or fully-centered state with hydrogen located at the midpoint of the hydrogen bond was observed by a neutron diffraction study. However, some subtle changes in Raman spectra indicated that the ordered symmetrization state might form at around 16 GPa.

Keywords: δ-AlOOH, phase transition, Raman spectra, luminescence, high pressure

1. Introduction

Hydrous minerals in subducted slabs are widely accepted as the dominant water carriers into the Earth's interior (Ohtani 2020). Their dehydration can significantly influence the evolution of the mantle by altering the physical and chemical properties of the surrounding materials (Hirschmann 2006; Mei and Kohlstedt 2000; Wang et al. 2006). To date, various hydrous minerals, such as antigorite, lawsonite and dense hydrous magnesium silicate phases, have been suggested to transport water from the Earth's surface to the deep mantle (Iwamori 2004; Ono 1998). Among those hydrous minerals, δ-AlOOH stands out due to its wide P-T stability field. High-pressure and high-temperature experiments have indicated that δ-AlOOH could survive P-T conditions up to ~140 GPa and 2500 K; hence this mineral is regarded as a potential water carrier to the Earth's core-mantle boundary (Duan et al. 2018; Ohtani et al. 2001; Piet et al. 2020). Since Suzuki et al. (2000) first synthesized it by the dehydration reaction of $Al(OH)_3$ at 21 GPa and 1000 °C, several routes have been proposed to produce δ-AlOOH using various starting materials including diaspore, phase egg and hydrous peridotite (Fukuyama et al. 2017; Ohtani et al. 2001; Sano et al. 2004; Yoshino et al. 2019; Zhang et al. 2019). These results have further confirmed the possible existence of δ-AlOOH in the deep interior of the Earth.

δ-AlOOH belongs to orthorhombic system with a $P2_1nm$ space group under ambient conditions (Komatsu et al. 2006). It consists of infinite edge-sharing AlO_6 octahedral chains along the *c*-axis that are cross-linked by hydrogen bonds in the *a*-*b* plane (Figure 1a). Due to its significance as an important water carrier at lower mantle

depths in subduction zones, the structural behavior of δ-AlOOH at high pressure has attracted much attention. X-ray diffraction studies observed a significant change in the axial ratios of *a/c* and *b/c* at ~10 GPa, which is likely to correspond to the structural transition from $P2_1nm$ to *Pnnm* (Kuribayashi et al. 2014; Sano-Furukawa et al. 2009; Simonova et al. 2020). An analysis of the unit-cell volume versus pressure data showed that the bulk modulus of the high-pressure *Pnnm* phase was ~52% higher than that of the low pressure $P2_1nm$ phase, indicating a stiffened unit cell after the phase transition (Simonova et al. 2020). Moreover, significant changes in the frequency slope with pressure for the vibrational modes related to hydrogen bonds were also indicated at ~10 GPa by IR spectroscopic measurements (Kagi et al. 2010). A recent neutron diffraction study further revealed that this structural transition is accompanied with the order-to-disorder transformation of hydrogen along hydrogen bonds as a result of the tunneling effect of hydrogen, and the high-pressure disordered phase further transitions into an ordered phase with symmetrized hydrogen bonds or fully-centered phase at ~18 GPa without changing the *Pnnm* structure; in this ordered phase, hydrogen atoms are located at the midpoints of two neighboring hydrogen-bonded oxygen atoms (Sano-Furukawa et al. 2018). However, the transition to the ordered symmetrization phase was not observed to relate to any unusual feature in previous X-ray diffraction or spectroscopic works (Kagi et al. 2010; Simonova et al. 2020). The structures of the disordered and ordered *Pnnm* phases are shown in Figure 1 (b) and Figure 1 (c), respectively. Additionally, first-principle calculations were used to understand these structural behaviors and their effect on the physical properties of

δ-AlOOH. These calculations have reproduced the primary experimental phenomena, such as changes in the compressibility of the axial ratios and pressure dependences of elastic moduli across the phase transition (Cedillo et al. 2016; Cortona 2017; Li et al. 2006; Pillai et al. 2018; Tsuchiya and Tsuchiya 2009). However, the critical pressure of ~30 GPa for hydrogen-bond symmetrization predicted in most theoretical studies was much higher than the experimental value of ~18 GPa (Sano-Furukawa et al. 2018; Tsuchiya et al. 2008). Moreover, the calculations completely missed the disordered phase in the structural transition path and hence ascribed the abnormal behaviors to the symmetrization of hydrogen bonds, which was not consistent with the neutron diffraction result of Sano-Furukawa et al. (2018). Although a comprehensive theoretical model has not yet been well depicted, one recent theoretical work showed that the disordered *Pnnm* phase of δ-AlOOH can be successfully described when thermal and nuclear quantum effects are considered (Bronstein et al. 2017).

It is well known that Raman and luminescence spectroscopies are sensitive to local bonding environments; hence it is possible to characterize the structural evolution of δ-AlOOH from a spectroscopic perspective. Indeed, one previous study by Mashino et al. (2016) already showed the disappearance and appearance of Raman peaks at 6.5 GPa, which were taken as the signatures for the $P2_1nm$-to-*Pnnm* phase transition. The observed critical pressure of 6.5 GPa in their study was slightly lower than that determined by X-ray and neutron diffraction studies; this discrepancy may be due to the existence of deviatoric stress in the sample because no pressure-transmitting medium was used in the experiments. Additionally, the

first-principle calculations of Tsuchiya et al. (2008) also showed that some lattice modes in the $P2_1nm$ phase exhibited softening behaviors with increasing pressure. However, no detailed Raman scattering study at high pressure has yet to be reported for δ-AlOOH. A previous Raman study recorded only a limited number of Raman modes (Mashino et al. 2016), and no softening behavior was clearly documented. Therefore, a further Raman study is still essential for better understanding the structural behavior and vibrational dynamics of δ-AlOOH under high pressure. In addition to Raman spectroscopy, luminescence spectroscopy of Cr^{3+} provides another effective method to probe the local structural information in minerals under high pressure. Ruby is a typical material of Cr^{3+} luminescence and is widely used as a pressure calibration in diamond-anvil cells by utilizing the pressure-induced shift of its R_1 emission line (Syassen 2008). Several recent studies have further certified that the luminescence of Cr^{3+} can be used as an indicator for subtle structural modification in minerals under high pressure (O'Bannon III and WIllIams 2019; O'Bannon and Williams 2016a, 2016b). To the best of our knowledge, this method has not been applied to investigate the compression behavior of δ-AlOOH thus far.

To further explore the structural evolution of δ-AlOOH upon compression by spectroscopic methods, we performed high pressure Raman scattering and luminescence spectroscopic measurements on single-crystal δ-AlOOH and Cr^{3+}-bearing powder δ-AlOOH. We mainly focused on the proposed phase transitions in the process of hydrogen-bond symmetrization and tried to identify the unique signatures of these phase transitions in the spectroscopy results.

2. Experimental methods

Two samples, single-crystal δ-AlOOH and Cr^{3+}-bearing powder δ-AlOOH, were synthesized under high pressure and high-temperature conditions on the Sakura 2500-ton multi-anvil apparatus at the Guangzhou Institute of Geochemistry, Chinese Academy of Sciences. The typical sample assembly for the synthesis of δ-AlOOH is the same as that described by Liu et al. (2019). For single-crystal δ-AlOOH, reagent grade $Al(OH)_3$ of high purity was used as the starting material and was placed in a welded gold capsule; the synthesis experiment was performed at 20 GPa and 1000 °C with a duration of 22 hours (run number U795). The recovered sample was composed of transparent crystals with maximum dimensions of approximately 300 μm. To synthesize Cr^{3+}-bearing powder δ-AlOOH, we utilized ground natural diaspore powder with strong Cr^{3+} luminescence as the starting material, and the P-T conditions for the synthesis were ~19 GPa and ~1000 °C (run number U765; the temperature was estimated from the heating power due to thermocouple cutoff during the experiment). The recovered sample contained fine-grained aggregates of δ-AlOOH. Both samples were confirmed to be a single phase of δ-AlOOH with a $P2_1nm$ structure by X-ray diffraction measurements at the 13IDD beamline of GSECARS. The lattice parameters were a = 4.7093(8) Å, b = 4.2271(1) Å, c = 2.8302(1) Å, and V_0 = 56.34(5) $Å^3$ for the single-crystal sample and a = 4.7136(1) Å, b = 4.2255(4) Å, c = 2.8329(1) Å, and V_0 =56.42 (4) $Å^3$ for the powder sample, which are very close to the values reported in a recent single-crystal X-ray diffraction study (Simonova et al. 2020). The chemical compositions determined by electron probe microanalysis (EPMA) indicate

that the single-crystal sample is of high purity, containing AlOOH with an ideal formula, while the powder sample contained small amounts of Fe_2O_3 (0.57 wt. %) and Cr_2O_3 (0.05 wt. %).

Raman scattering and luminescence spectroscopy measurements were performed for both the single-crystal and powder δ-AlOOH samples at ambient conditions and under high pressures. The high pressures were generated by a short symmetric diamond-anvil cell with a culet size of 400 μm. A piece of double-polished δ-AlOOH single-crystal or a flat powder δ-AlOOH pellet was loaded into the sample chamber drilled in a pre-indented Re gasket. Argon was loaded to serve as a pressure-transmitting medium by the cryogenic method. The pressure was determined by the traditional ruby fluorescence method (Mao et al. 1986). The Raman scattering and luminescence spectra were collected with a resolution of 1-2 cm^{-1} using an InVia Renishaw Raman spectrometer for powder δ-AlOOH and a WITec Raman spectrometer for single-crystal δ-AlOOH, respectively. The wavelength of the laser for both Raman systems was 532 nm. The obtained spectra were fitted by Horiba Scientific LabSpec 5 software to extract the peak positions.

3. Results and Discussions

3.1 Raman and luminescence spectra at ambient conditions

The Raman spectra of the single-crystal and powder δ-AlOOH collected under ambient conditions are shown in Figure 2. The spectral profiles of the two samples are quite similar in the lattice vibration region ranging from 100-1400 cm^{-1}. A factor

group analysis predicted 21 Raman-active modes ($\Gamma = 7A_1+4A_2+3B_1+7B_2$) for δ-AlOOH (Tsuchiya et al. 2008). However, we only observed 9 modes due to the weak intensities of the other modes or due to vibrational peak overlapping. The peak fitting results indicated that the observed modes for both samples were almost the same in frequency within errors; therefore, we listed the frequency values in Figure 2 without distinguishing the samples. The symmetry of each mode was also labeled according to the first-principle calculations by Tsuchiya et al. (2008). As it was difficult to assign symmetry accurately based only on the calculated frequency when several peaks were very close together in frequency, we carefully traced the evolution of the modes with pressure and compared them with the simulated results to avoid potential mistakes. The B_2 mode at 1340 cm^{-1} can be assigned as originating from the bending vibration of the O-H···O hydrogen bonds. The modes between 276 and 620 cm^{-1} can be attributed to the vibrations of the AlO_6 octahedron (Xue et al. 2006). In particular, the A_1 mode at 276 cm^{-1} and the B_2 mode at 382 cm^{-1} correspond to lattice vibrations that are correlated with the O-H stretching vibrations of hydrogen bonds (Tsuchiya et al. 2008).

In the O-H stretching vibration region, no peaks can be distinguished for the powder δ-AlOOH sample due to the strong luminescence of Cr^{3+} (Figure 2). However, broad multibands existed for the single-crystal δ-AlOOH sample. According to the correlation between the O-H stretching frequency and O-H···O bond distance proposed by Libowitzky (1999), we derived that the O-O distance ranges from 2.52 Å to 2.63 Å, which is close to the value of 2.55 Å determined by X-ray diffraction

measurements (Kuribayashi et al. 2014). To date, the origin of these multibands is still under debate, and has been either ascribed to either Fermi resonance by Xue et al. (2006) or disorder superstructure by Tsuchiya et al. (2008). We found that the disorder model of Tsuchiya et al. (2008) can reproduce the Raman spectra collected in our present experiments well.

In the luminescence spectra (Figure 3), the most prominent feature of the powder δ-AlOOH was two sharp and strong peaks at 684.2 nm and 686.5 nm, which can be undoubtedly assigned to the R_1 and R_2 lines of Cr^{3+} luminescence. The R-lines originate from the spin-forbidden ^2E-$^4A_2$ transition of Cr^{3+} and imply a relatively strong octahedral crystal field of CrO_6 in δ-AlOOH (Tanabe and Sugano 1954). Even though no Cr^{3+} was detected by EPMA in the crystal δ-AlOOH, the sample displays a luminescence spectrum very similar to that of the powder δ-AlOOH sample, implying that a minor amount of Cr^{3+} was incorporated in the crystal δ-AlOOH sample. We speculate that the minor Cr^{3+} in the crystal δ-AlOOH was likely introduced by the $LaCrO_3$ heater during the high-pressure and high-temperature synthesis experiment using the multi-anvil apparatus, which was also observed in the synthesis experiment of Si-rich Mg-sursassite (Bindi et al. 2020). Based on the EPMA data, a small amount of Fe_2O_3 is present in the powder δ-AlOOH; however, it seems that no obvious luminescence peaks result from this Fe^{3+} due to the similarity of the luminescence spectra of the two samples. Additionally, several sidebands are observed on both sides of the R-lines. The sidebands may be associated with Cr^{3+}pairs or vibronic peaks (O'Bannon and Williams 2016a, 2016b). All the luminescence peak positions are

given in Table 1.

3.2 High pressure Raman spectra

Raman spectra were collected at high pressures up to 34 GPa for the powder δ-AlOOH and up to 34.6 GPa for the single-crystal δ-AlOOH. The stacked representative Raman spectra are shown in Figure 4. Due to the strong first-order Raman peak of diamond at ~1300 cm^{-1}, our Raman scattering measurements at high pressures were restricted to a wavenumber region from ~100 cm^{-1} to 1200 cm^{-1}. Although the OH stretching vibrational modes for single-crystal δ-AlOOH were clearly recorded under ambient conditions, they were unable to be observed at high pressures due to the interference of the second-order Raman peaks of diamond at ~2600 cm^{-1}. Therefore, the Raman-active O-H···O bending and OH stretching vibrational modes, which are in the wavenumber ranges of 1200–1400 cm^{-1} and 2000–3000 cm^{-1} respectively, were not investigated at high pressures in this study. Fortunately, we were able to clearly observe at least six lattice vibrational modes in the collected high-pressure Raman spectra, allowing us to trace the compression behavior of δ-AlOOH.

The powder and single-crystal δ-AlOOH samples exhibit similar spectral features and evolution with pressure. The lowest A_1 mode at 276 cm^{-1} shifts quickly to a low wavenumber with the broadening peak width and gradually decreasing intensity as the pressure increases. The B_2 mode at 382 cm^{-1} also shows a negative pressure dependence but disappears at 6.5 GPa. In contrast to the softening behavior of the 276

235 cm^{-1} A_1 and 382 cm^{-1} B_2 modes, the B_2 modes at 390 cm^{-1} and 416 cm^{-1} shift toward
236 high wavenumbers with increasing pressure. The A_1 mode at ~515 cm^{-1} is not
237 sensitive to pressure and the B_2 mode at 626 cm^{-1} shows a weak negative response to
238 pressure. At pressures of 8.1 GPa and above, only two of six initial peaks can be
239 observed, and several new weak peaks gradually appear. The detailed evolution trends
240 of these modes are marked by red dashed lines in Figure 4.

241 The frequencies of the vibrational modes are plotted as a function of pressure in
242 Figure 5, together with the previous data of Mashino et al. (2016). Clearly, the B_2
243 modes at 390 cm^{-1} and 416 cm^{-1} show abrupt changes in their pressure dependences at
244 ~8 GPa, indicating the $P2_1nm$-to-$Pnnm$ phase transition observed in previous
245 diffraction studies (Sano-Furukawa et al. 2018; Sano-Furukawa et al. 2009; Simonova
246 et al. 2020). In the pressure range of 0-8 GPa, these two modes increase rapidly with
247 pressure and display nonlinear behavior. Above 8 GPa, the modes exhibit less
248 sensitivity to pressure with smaller linear slopes. In the case of the four softening
249 modes, the A_1 mode at 276 cm^{-1} and B_2 mode at 382 cm^{-1}, which correspond to the
250 lattice vibrations of AlO_6 correlated with the OH stretching vibration, are found to be
251 highly sensitive to pressure with respect to the other two B_2 softening modes at 515
252 cm^{-1} and 626 cm^{-1}. The frequency of the B_2 mode decreases from 382 cm^{-1} under
253 ambient pressure to 346 cm^{-1} at 5.5 GPa and the A_1 mode decreases from 276 cm^{-1} at
254 ambient conditions to ~74 cm^{-1} at 7.4 GPa. It is obvious that the negative slopes
255 become larger with increasing pressure. Given the many pressure points, the shift of
256 the A_1 soft mode at 276 cm^{-1} with pressure is fitted using the quadratic polynomial

function. The best fitting shows that the frequency of the A_1 mode reaches 0 cm^{-1} at ~9 GPa (see the inset of Figure 5), which is very close to the pressure of the $P2_1nm$-to-$Pnnm$ phase transition. We noticed that one new peak at 701 cm^{-1} appears at 9 GPa for powder δ-AlOOH; this peak may be related to the phase transition. Additionally, another new weak peak at 616 cm^{-1} was observed at 13.1 GPa for crystal δ-AlOOH, and some new peaks are more clear at pressures of 16.5 GPa and above. A recent neutron diffraction study indicated that the hydrogen-bond symmetrization of δ-AlOOH took place at ~18 GPa. We speculate that the appearance of these news peaks might correlate with the process of hydrogen-bond symmetrization from the disordered state to the ordered state of hydrogen.

3.3 High pressure luminescence spectra

Luminescence spectroscopic measurements were performed at pressures up to 22.1 GPa for both the powder and single-crystal δ-AlOOH samples (Figure 6 and Figure 7). Because the sidebands of the single-crystal δ-AlOOH were very weak due to the low Cr^{3+} content, only the R-lines were clearly discerned for the spectra at high pressures (Figure 7). In contrast, the sidebands and R-lines of the powder δ-AlOOH could be traced up to the maximum pressure. The luminescence spectra of δ-AlOOH at selected pressures are depicted in Figure 6. The relative intensity of the R-lines to the sidebands gradually deceases with increasing pressure and the R_1 and R_2 lines gradually converge into a single peak. At pressures of 13.4 GPa and above, it became difficult to deconvolve the R-lines with two peaks. The obtained peak positions for the emission lines at different pressures for both samples are shown in Figure 8. One

key feature is the nonlinear behavior that shows kinks at ~8 GPa. For example, R_1 remains at a nearly constant wavelength with increasing pressure below 8 GPa and then increases rapidly at pressures above 8 GPa. The slopes or pressure dependences of the sidebands and R-lines were calculated for the pressure regions below and above 8 GPa respectively, and are listed in Table 1. The anomalous variation in the slopes of the sidebands and R-lines is not surprising since a phase transition has been suggested to take place at the same pressure (Kuribayashi et al. 2014; Sano-Furukawa et al. 2018). Therefore, our luminescence spectra provide additional clear evidence for the structural transition from $P2_1nm$ to $Pnnm$ in δ-AlOOH. Similar to our Raman experiments, no obvious change in the pressure dependence of the wavelengths of the sidebands or R-lines was observed at ~18 GPa.

The R-lines of Cr^{3+} correspond to the environment of the Al site in the crystal structure of δ-AlOOH, and R_2-R_1 splitting is regarded as an indicator of the distortion of the AlO_6 octahedron (O'Bannon III and WIllIams 2019; O'Bannon and Williams 2016a, 2016b). Generally, a highly-distorted AlO_6 octahedron leads to a large R_2-R_1 splitting. Here, we plotted the R_2-R_1 splitting as a function of pressure in Figure 9 (a). The R_2-R_1 separation decreases continuously with pressure, implying that the AlO_6 octahedron becomes less distorted under compression. From previous X-ray diffraction studies on the ordered asymmetrical $P2_1nm$ phase under ambient conditions, two different oxygen sites exist in a selected AlO_6 octahedron of δ-AlOOH based on their relation to hydrogen. The O1 is linked to hydrogen by a weak H···O hydrogen bond, and the O2 forms covalent bonds with hydrogen

(Komatsu et al. 2006). As shown in Figure 9 (b), we label O1a and O2a for oxygen atoms in the axial positions and O1e and O2e for oxygen atoms in the equatorial positions. In the high-pressure phase with symmetrical hydrogen-bonds (the ordered symmetrization phase), Al shifts to the center of an AlO_6 octahedron, and four Al-O bonds in the equatorial plane become equal in bond length (Figure 9 (c)); hence, the distortion of the AlO_6 octahedron is expected to be suppressed. According to the method proposed by Robinson et al. (1971), quadratic elongation (QE), the distortion factor of the AlO_6 octahedron, was calculated using VESTA software with the structural data reported by previous diffraction studies (Momma and Izumi 2008; Sano-Furukawa et al. 2018; Simonova et al. 2020). As shown in the inset of Figure 9 (a), the QE value, which is 1.0071 at ambient conditions, drops to 1.0033 at ~8 GPa after the phase transition from the $P2_1nm$ to the *Pnnm* structure, indicating that pressure-induced suppression of distortion in the AlO_6 octahedron occurs during the phase transition and further verifying further the conclusion inferred from R-lines splitting.

3.4 Structural behavior and hydrogen-bond symmetrization in δ-AlOOH

δ-AlOOH possesses a distorted rutile-type structure ($P2_1nm$) with a strong and asymmetrical hydrogen bond under ambient conditions (Komatsu et al. 2006) and is predicted to transition into the *Pnnm* structure with symmetrical hydrogen bonds under compression (Tsuchiya et al. 2008). The abnormal change in the compressibility of δ-AlOOH that has been observed at ~10 GPa by X-ray diffraction experiments in the past decade was correlated with hydrogen-bond symmetrization by

Sano-Furukawa et al. (2009). However, most theoretical studies have predicted a much higher critical pressure of ~30 GPa for hydrogen-bond symmetrization in δ-AlOOH (Bronstein et al. 2017; Cedillo et al. 2016; Cortona 2017; Pillai et al. 2018; Tsuchiya and Tsuchiya 2009; Tsuchiya et al. 2008). Later X-ray diffraction studies indicated that the abnormal change in the compressibility of δ-AlOOH is related to the $P2_1nm$-to-$Pnnm$ phase transition in fact (Kuribayashi et al. 2014; Simonova et al. 2020). More recently, a neutron diffraction study revealed that δ-AlOOH undergoes the $P2_1nm$-to-$Pnnm$ transition at ~9 GPa, that this transition is coupled with the order-disorder transition of hydrogen along the hydrogen bonds due to tunneling effect, and that the transition to the ordered symmetrization phase occurs at ~18 GPa (Sano-Furukawa et al. 2018). The difference in pressure of the hydrogen bond symmetrization between the neutron diffraction study (Sano-Furusawa et al. 2018) and the theoretical study by Tsuchiya et al. (2008) can be explained well as a result of the temperature effect (Kang et al. 2017).

The Raman and luminescence spectral changes of δ-AlOOH at ~8 GPa observed in this study agree well with the $P2_1nm$-to-$Pnnm$ structure transition reported by previous X-ray and neutron diffraction studies (Kuribayashi et al. 2014; Sano-Furukawa et al. 2018; Simonova et al. 2020). In the low-pressure $P2_1nm$ phase with ordered asymmetrical hydrogen bonds, the softening behavior of the four Raman lattice modes reflects the pressure-induced evolution of the hydrogen-bond geometry in the process of hydrogen-bond symmetrization, i.e., the covalent O-H bondlength slightly increases while the O-H···O distance becomes shortened under compression.

In contrast to the softening behavior, the B_2 modes at 390 cm^{-1} and 416 cm^{-1} show rapid increases with pressure that are consistent with the high compressibility or low bulk modulus of the $P2_1nm$ phase. For the *Pnnm* phase, all the observed Raman modes exhibit less sensitivity in frequency to pressure with small linear slopes (Figure 5), which is consistent with the low compressibility or high bulk modulus of this phase (Sano-Furukawa et al. 2009; Simonova et al. 2020). It is interesting that the A_1 soft mode at 276 cm^{-1} was extrapolated to approach 0 cm^{-1} at ~9 GPa. Tsuchiya et al. (2008) indeed predicted by first-principle calculations that this mode will become 0 cm^{-1} when hydrogen-bond symmetrization takes place at 30 GPa. It is also noteworthy that the A_1 softening mode at 276 cm^{-1} vanishes before reaching 0 cm^{-1} at ~9 GPa, but the $P2_1nm$-to-*Pnnm* transition takes place at ~8 GPa. We speculate that the vanishing of the A_1 soft mode at 276 cm^{-1} is due to the much longer timespan of the Raman measurements than the quantum tunneling effect of hydrogen (proton) along the hydrogen bonds in δ-AlOOH; hence, the $P2_1nm$-to-*Pnnm* structure transition is predicted to be coupled with an order-disorder transition of hydrogen due to tunneling effect (Benoit et al. 1996; Sano-Furukawa et al. 2018).

Additionally, we did not notice significant changes in the pressure dependence (slope) of frequency for the Raman-active lattice modes or the emission R-lines or sidebands of δ-AlOOH at ~18 GPa, at which the hydrogen bonds change from a disordered state to an ordered symmetrization state with a single-well proton (hydrogen) potential, as observed by a recent neutron diffraction study (Sano-Furukawa et al. 2018). Similarly, previous IR spectroscopy and single-crystal

diffraction studies also did not show any unusual behavior at approximately 18 GPa (Kagi et al. 2010; Simonova et al. 2020). However, our Raman spectroscopic results do show some subtle changes that may be related to the transition from the disordered to ordered symmetrization state of hydrogen. In comparison with the 10.5 GPa spectrum of single-crystal δ-AlOOH, which can be assigned to be in the hydrogen-disordered state, several new but very weak peaks appear in the 16.5 GPa spectrum, and these new peaks become more clear at pressures of 24.4 GPa and above (Figure 4b). However, in comparison with the $P2_1nm$-to-$Pnnm$ transition, we noticed that the disordered-ordered symmetrization transition shows no obvious changes in the Raman scattering spectra. This might be determined by the nature of this phase transition (second-order), which is only related to the motion of hydrogen (proton) along hydrogen bonds from the disordered state to the fully-centered state with hydrogen located at the midpoint of a hydrogen bond. Both the neutron diffraction and Brillouin scattering evidence support the existence of a disordered-to-ordered symmetrization transition at pressures of approximately 15-20 GPa (Mashino et al. 2016; Sano-Furukawa et al. 2018; Su et al. 2021b). Theoretical studies predicted that thermal and quantum effects may play important roles in the process of hydrogen-bond symmetrization (Bronstein et al. 2017; Kang et al. 2017). The ab initio molecular dynamics calculations with finite-temperature statistics yielded that the transition pressure to the ordered hydrogen-bond symmetrization state was 17.0 GPa at 300 K, being in good agreement with the neutron diffraction study and our present study (Kang et al. 2017; Sano-Furukawa et al. 2018).

4. Implications

The Hydrogen-bond geometry and its evolution with pressure have profound effect on the structural behaviour and physical property of δ-AlOOH and other hydrous minerals, especially elasticity (Mashino et al. 2016; Tsuchiya and Tsuchiya 2009). First-principles calculations by Tsuchiya and Tsuchiya (2009) predicted that the elastic constants of δ-AlOOH with asymmetrical hydrogen bonds (the ordered asymmetrical $P2_1nm$ phase) are significantly smaller than those of δ-AlOOH with symmetrical hydrogen bonds. In the process of hydrogen-bond symmetrization of δ-AlOOH, the diagonal elastic constants (especially C_{11} and C_{22}), the bulk and shear moduli, and the acoustic velocities (V_P, V_S) show an anomalous increase or harden rapidly with pressure, and then become stiffened after achieving the ordered symmetrization state. These theoretical predictions have been confirmed by high-pressure Brillouin scattering experiments on δ-AlOOH polycrystalline aggregate (Mashino et al. 2016; Su et al. 2021b). Besides, according to the phase diagram of AlOOH (Yoshino et al. 2019), the hydrogen-bond symmetrization is inferred to promote the stability field (or dehydration temperature) of δ-AlOOH.

Phase relation and stability experiments revealed that δ-AlOOH is an important hydrous mineral as the decomposition product of phase egg in the sedimentary layer of subducted slabs (Ono et al. 1998; Sano et al. 2004; Fukuyama et al. 2017), and may even exist in the basaltic and ultramafic layers (Suzuki et al. 2000; Ohtani et al. 2001; Yuan et al. 2019). It is stable under the P-T conditions of the lower part of the mantle transition zone and the lower mantle (Sano et al. 2004; Fukuyama et al. 2017; Duan et

al. 2018; Yuan et al. 2019). According to our Raman and luminescence results, δ-AlOOH under compression undergoes hydrogen-bond symmetrization and achieves the ordered symmetrization state at ~16 GPa. Because quantum effects of hydrogen is predicted to dominate the process of hydrogen-bond symmetrization (Bronstein et al. 2017), a weak temperature dependence of the transition pressure to the ordered symmetrization phase is expected. Therefore, it can be estimated that δ-AlOOH is generally in the ordered symmetrization state in the Earth's deep interior. The compressional-wave (V_P) and shear-wave (V_S) velocities of δ-AlOOH in the ordered symmetrization phase are significantly greater than most major minerals in the mantle transition zone and low mantle bridgemanite and hence may contribute to the high-velocity seismic anomalies at depths of the mantle transition zone and upmost low mantle (Su et al. 2021b).

In contrast to δ-AlOOH, other subduction-related hydrous minerals, such as ε-FeOOH, phase D and ice VII, transit to the disordered phase and the ordered symmetrization phase at pressures higher than their lower pressure limits of stability fields (Guthrie et al. 2019; Thompson et al. 2020; Tsuchiya et al. 2005; Yoshino et al. 2019). These hydrous minerals may vary from ordered asymmetrical, disordered and ordered symmetrization states of hydrogen bond with increasing depth in the Earth's deep interior. To constrain well geophysical observations so as to understand the water storage and circulation in subduction zones, it is essential to investigate systematically the effect of hydrogen-bond symmetrization on the physical property of subduction-related hydrous minerals by both high-pressure experiments and

theoretical calculations.

Under nature circumstances, δ-AlOOH in the basaltic and ultramafic layers of subducting slabs may contain some amount of iron (Yuan et al. 2019). The incorporation of iron can significantly increase the $P2_1nm$-$Pnnm$ transition and hydrogen-bond symmetrization pressures of δ-AlOOH, decrease its acoustic velocities and affect other physical properties such as electrical conductivity and thermal conductivity (Su et al. 2021a, 2021b). Especially, the iron in δ-AlOOH can induce the high spin to low spin transition at high pressure. Therefore, it is also necessary to figure out in details the effect of iron on the physical property of δ-AlOOH in future.

Acknowledgments

We would like to thank Eiichi Takahashi for his technical assistance in the sample synthesis. The X-ray diffraction measurements of samples under ambient conditions were conducted at the 13-IDD beamline of GSECARS, Advanced Photon Source, Argonne National Laboratory. GSECARS is supported by the National Science Foundation-Earth Sciences (EAR-1634415) and Department of Energy-GeoSciences (DEFG02-94ER14466). This research was financially supported by the Strategic Priority Research Program (B) of the Chinese Academy of Sciences (Grant No. XDB18000000) and the National Natural Science Foundation of China (Grants No. 41874107, 41574079). This is contribution No. IS-XXXX from GIGCAS.

References

Benoit, M., Marx, D., and Parrinello, M. (1998) Tunneling and zero-point motion in

high-pressure ice. Nature, 392,258-261.

Bindi, L., Welch, M.D., Bendeliani, A.A., and Bobrov, A.V. (2020) Si-rich Mg-sursassite $Mg_4Al_5Si_7O_{23}$ $(OH)_5$ with octahedrally coordinated Si: A new ultrahigh-pressure hydrous phase. American Mineralogist, 105(9), 1432-1435.

Bronstein, Y., Depondt, P., and Finocchi, F. (2017) Thermal and nuclear quantum effects in the hydrogen bond dynamical symmetrization phase transition of δ-AlOOH. European Journal of Mineralogy, 29(3), 385-395.

Cedillo, A., Torrent, M., and Cortona, P. (2016) Stability of the different AlOOH phases under pressure. Journal of Physics: Condensed Matter, 28(18), 185401.

Cortona, P. (2017) Hydrogen bond symmetrization and elastic constants under pressure of δ-AlOOH. Journal of Physics: Condensed Matter, 29(32), 325505.

Duan, Y., Sun, N., Wang, S., Li, X., Guo, X., Ni, H., Prakapenka, V.B., and Mao, Z. (2018) Phase stability and thermal equation of state of δ-AlOOH: Implication for water transportation to the Deep Lower Mantle. Earth and Planetary Science Letters, 494, 92-98.

Fukuyama, K., Ohtani, E., Shibazaki, Y., Kagi, H., and Suzuki, A. (2017) Stability field of phase Egg, $AlSiO_3OH$ at high pressure and high temperature: possible water reservoir in mantle transition zone. Journal of Mineralogical and Petrological Sciences, 112(1), 31-35.

Guthrie, M., Boehler, R., Molaison, J.J., Haberl, B., dos Santos, A., and Tulk, C. (2019) Structure and disorder in ice VII on the approach to hydrogen-bond symmetrization. Physical Review B, 99(18), 184112.

476 Hirschmann, M.M. (2006) Water, melting, and the deep Earth H_2O cycle. Annu. Rev.
477 Earth Planet. Sci., 34, 629-653.
478 Iwamori, H. (2004) Phase relations of peridotites under H_2O-saturated conditions and
479 ability of subducting plates for transportation of H_2O. Earth and Planetary
480 Science Letters, 227(1-2), 57-71.
481 Kagi, H., Ushijima, D., Sano-Furukawa, A., Komatsu, K., Iizuka, R., Nagai, T., and
482 Nakano, S. (2010) Infrared absorption spectra of δ-AlOOH and its deuteride at
483 high pressure and implication to pressure response of the hydrogen bonds.
484 Journal of Physics: Conference Series, 215, p. 012052. IOP Publishing.
485 Kang, D., Feng, Y.-X., Yuan, Y., Ye, Q.-J., Zhu, F., Huo, H.-Y., Li, X.-Z., and Wu, X.
486 (2017) Hydrogen-bond symmetrization of δ-AlOOH. Chinese Physics Letters,
487 34(10), 108301.
488 Komatsu, K., Kuribayashi, T., Sano, A., Ohtani, E., and Kudoh, Y. (2006)
489 Redetermination of the high-pressure modification of AlOOH from single-crystal
490 synchrotron data. Acta Crystallographica Section E: Structure Reports Online,
491 62(11), i216-i218.
492 Kuribayashi, T., Sano-Furukawa, A., and Nagase, T. (2014) Observation of
493 pressure-induced phase transition of δ-AlOOH by using single-crystal
494 synchrotron X-ray diffraction method. Physics and Chemistry of Minerals, 41(4),
495 303-312.
496 Li, S., Ahuja, R., and Johansson, B. (2006) The elastic and optical properties of the
497 high-pressure hydrous phase δ-AlOOH. Solid State Communications, 137(1-2),

101-106.

Libowitzky, E. (1999) Correlation of OH stretching frequencies and OH… O hydrogen bond lengths in minerals. Monatshefte für Chemie/Chemical Monthly, 130(8), 1047-1059.

Liu, X., Matsukage, K.N., Nishihara, Y., Suzuki, T., and Takahashi, E. (2019) Stability of the hydrous phases of Al-rich phase D and Al-rich phase H in deep subducted oceanic crust. American Mineralogist: Journal of Earth and Planetary Materials, 104(1), 64-72.

Mao, H., Xu, J.-A., and Bell, P. (1986) Calibration of the ruby pressure gauge to 800 kbar under quasi-hydrostatic conditions. Journal of Geophysical Research: Solid Earth, 91(B5), 4673-4676.

Mashino, I., Murakami, M., and Ohtani, E. (2016) Sound velocities of δ-AlOOH up to core-mantle boundary pressures with implications for the seismic anomalies in the deep mantle. Journal of Geophysical Research: Solid Earth, 121(2), 595-609.

Mei, S., and Kohlstedt, D.L. (2000) Influence of water on plastic deformation of olivine aggregates: 1. Diffusion creep regime. Journal of Geophysical Research: Solid Earth, 105(B9), 21457-21469.

Momma, K., and Izumi, F. (2008) VESTA: a three-dimensional visualization system for electronic and structural analysis. Journal of Applied Crystallography, 41(3), 653-658.

O'Bannon III, E.F., and WIllIams, Q. (2019) A Cr^{3+} luminescence study of natural topaz Al_2SiO_4 (F, OH) $_2$ up to 60 GPa. American Mineralogist: Journal of Earth

and Planetary Materials, 104(11), 1656-1662.

O'Bannon, E., and Williams, Q. (2016a) Beryl-II, a high-pressure phase of beryl: Raman and luminescence spectroscopy to 16.4 GPa. Physics and Chemistry of Minerals, 43(9), 671-687.

O'Bannon III, E., and Williams, Q. (2016b) A Cr^{3+} luminescence study of spodumene at high pressures: Effects of site geometry, a phase transition, and a level-crossing. American Mineralogist, 101(6), 1406-1413.

Ohtani, E. (2020) The role of water in Earth's mantle. National Science Review, 7(1), 224-232.

Ohtani, E., Litasov, K., Suzuki, A., and Kondo, T. (2001) Stability field of new hydrous phase, δ-AlOOH, with implications for water transport into the deep mantle. Geophysical Research Letters, 28(20), 3991-3993.

Ono, S. (1998) Stability limits of hydrous minerals in sediment and mid-ocean ridge basalt compositions: Implications for water transport in subduction zones. Journal of Geophysical Research: Solid Earth, 103(B8), 18253-18267.

Piet, H., Leinenweber, K.D., Tappan, J., Greenberg, E., Prakapenka, V.B., Buseck, P.R., and Shim, S.-H. (2020) Dehydration of δ-AlOOH in Earth's Deep Lower Mantle. Minerals, 10(4), 384.

Pillai, S.B., Jha, P.K., Padmalal, A., Maurya, D., and Chamyal, L. (2018) First principles study of hydrogen bond symmetrization in δ-AlOOH. Journal of Applied Physics, 123(11), 115901.

Robinson, K., Gibbs, G., and Ribbe, P. (1971) Quadratic elongation: a quantitative

measure of distortion in coordination polyhedra. Science, 172(3983), 567-570.

Sano, A., Ohtani, E., Kubo, T., and Funakoshi, K. (2004) In situ X-ray observation of decomposition of hydrous aluminum silicate $AlSiO_3OH$ and aluminum oxide hydroxide δ-AlOOH at high pressure and temperature. Journal of Physics and Chemistry of Solids, 65, 1547–1554.

Sano-Furukawa, A., Hattori, T., Komatsu, K., Kagi, H., Nagai, T., Molaison, J.J., dos Santos, A.M., and Tulk, C.A. (2018) Direct observation of symmetrization of hydrogen bond in δ-AlOOH under mantle conditions using neutron diffraction. Scientific reports, 8(1), 1-9.

Sano-Furukawa, A., Kagi, H., Nagai, T., Nakano, S., Fukura, S., Ushijima, D., Iizuka, R., Ohtani, E., and Yagi, T. (2009) Change in compressibility of δ-AlOOH and δ-AlOOD at high pressure: A study of isotope effect and hydrogen-bond symmetrization. American Mineralogist, 94(8-9), 1255-1261.

Simonova, D., Bykova, E., Bykov, M., Kawazoe, T., Simonov, A., Dubrovinskaia, N., and Dubrovinsky, L. (2020) Structural study of δ-AlOOH up to 29 GPa. Minerals, 10(12), 1055.

Su,X., Zhao, C., Xu L., Lv, C., Song, X., Ishii,T., Xiao, Y., Chow, P., Sun, Q., Liu, J. (2021a) Spectroscopic evidence for the Fe^{3+} spin transition in iron-bearing δ-AlOOH at high pressure. American Mineralogist, 106: 10.2138/am-2021-7541.

Su, X., Zhao, C., Lv, C., Zhuang, Y., Salke, N. P., Xu, L., Tang, H., Gou, H., Yu, X., Sun, Q., Liu, J. (2021b) The effect of iron on sound velocities of δ-AlOOH up to 135 GPa. Geoscience Frontiers, 12, 937-946.

564 Suzuki, A., Ohtani, E., and Kamada, T. (2000) A new hydrous phase δ-AlOOH
565 synthesized at 21 GPa and 1000 C. Physics and Chemistry of Minerals, 27(10),
566 689-693.
567 Syassen, K. (2008) Ruby under pressure. High Pressure Research, 28(2), 75-126.
568 Tanabe, Y., and Sugano, S. (1954) On the absorption spectra of complex ions II.
569 Journal of the Physical Society of Japan, 9(5), 766-779.
570 Thompson, E., Davis, A., Brauser, N., Liu, Z., Prapapenka, V., Campbell, A. (2020)
571 Phase transitions in ε-FeOOH at high pressure and ambient temperature.
572 American Mineralogist, 105,1769-1777.
573 Tsuchiya, J., and Tsuchiya, T. (2009) Elastic properties of δ-AlOOH under pressure:
574 First principles investigation. Physics of the Earth and planetary interiors,
575 174(1-4), 122-127.
576 Tsuchiya, J., Tsuchiya, T., and Tsuneyuki, S. (2005) First-principles study of hydrogen
577 bond symmetrization of phase D under high pressure. American Mineralogist,
578 90(1), 44-49.
579 Tsuchiya, J., Tsuchiya, T., and Wentzcovitch, R.M. (2008) Vibrational properties of
580 δ-AlOOH under pressure. American Mineralogist, 93(2-3), 477-482.
581 Wang, D., Mookherjee, M., Xu, Y., and Karato, S.-i. (2006) The effect of water on the
582 electrical conductivity of olivine. Nature, 443(7114), 977-980.
583 Xue, X., Kanzaki, M., Fukui, H., Ito, E., and Hashimoto, T. (2006) Cation order and
584 hydrogen bonding of high-pressure phases in the Al_2O_3-SiO_2-H_2O system: An
585 NMR and Raman study. American Mineralogist, 91(5-6), 850-861.

586 Yoshino, T., Baker, E., and Duffey, K. (2019) Fate of water in subducted hydrous
587 sediments deduced from stability fields of FeOOH and AlOOH up to 20 GPa.
588 Physics of the Earth and Planetary Interiors, 294, 106295.
589 Yuan, H., Zhang L., Ohtani, E., Meng, Y., Greenberg, E., Prakapenka, V. (2019)
590 Stability of Fe-bearing hydrous phases and element partitioning in the system
591 $MgO–Al_2O_3–Fe_2O_3–SiO_2–H_2O$ in Earth's lowermost mantle. Earth and Planetary
592 Science letters, 524,115714.
593 Zhang, L., Smyth, J.R., Kawazoe, T., Jacobsen, S.D., Niu, J., He, X., and Qin, S.
594 (2019) Stability, composition, and crystal structure of Fe-bearing Phase E in the
595 transition zone. American Mineralogist, 104(11), 1620-1624.
596
597
598
599
600
601
602
603
604
605

606

607

608

609

610

611

612

613 **Table 1.** The Cr^{3+} luminescence peak positions of δ-AlOOH under ambient conditions

614 and their slopes under compression.

615

No.	Ambient λ (nm)	$P2_1nm$ (0-8 GPa)	$Pnnm$ (8-22 GPa)
p1	661.3	0.17	0.12
p2	666.2	0.29	0.18
p3	669.1	0.12	-
p4	672.4	0.09	0.14
p5	673.4	0.35	0.09
p6	675.4	-	-
R_2	684.2	0.17	0.23

R_1	686.5	0.00	0.22
p7	698.4	0.08	0.35
p8	702.0	-	-
p9	705.0	0.10	0.33
p10	709.0	-	-
p11	711.6	0.21	0.49
p12	714.3	-	-
p13	717.4	0.45	0.49
p14	720.4	-	-

616

617 **Figure captions**

618 **Figure 1.** Crystal structures of δ-AlOOH. (a) The low pressure ordered $P2_1nm$ phase
619 with asymmetrical hydrogen bonds from ambient pressure to 8 GPa,, (b)
620 high-pressure disordered *Pnnm* phase with symmetrical hydrogen bonds from 8 to 18
621 GPa, and (c) high-pressure ordered *Pnnm* phase with symmetrical hydrogen bonds
622 above 18 GPa. The large silver, medium-red and small white spheres represent Al, O
623 and H atoms, respectively. The structures were drawn using VESTA software
624 (Momma and Izumi 2008). Structural data are from Sano-Furukawa et al. (2018).

625

626 **Figure 2.** Raman spectra of powder and crystal δ-AlOOH under ambient condition.

627

628 **Figure 3.** Luminescence spectra of powder and crystal δ-AlOOH under ambient

conditions. The inset shows the R_1 and R_2 values of Cr^{3+} luminescence in δ-AlOOH.

Figure 4. Representative high-pressure Raman spectra of δ-AlOOH in the (a) powder sample and (b) crystal sample. The red dashed lines trace the evolution of Raman peaks with increasing pressure.

Figure 5. The Raman mode frequencies of δ-AlOOH as a function of pressure. The black vertical dashed line indicates the phase transition at ~8 GPa from $P2_1nm$ to *Pnnm.* The black dashed lines below 8 GPa show the nonlinear evolution of the mode with pressure. The black solid lines above 8 GPa show the linear fitting results of the compressional data and the slopes are shown near the lines. The inset shows the quadratic polynomial extrapolation of the A_1 mode at 276 cm^{-1}.

Figure 6. Stacked high-pressure Cr^{3+} luminescence spectra of powder δ-AlOOH. The # denotes the R-line for ruby.

Figure 7. Stacked high-pressure Cr^{3+} luminescence spectra of crystal δ-AlOOH.

Figure 8. The Cr^{3+} luminescence peak positions of δ-AlOOH as a function of pressure. The black vertical dashed line indicates the phase transition from $P2_1nm$ to *Pnnm.* The blue solid lines are the linear fitting results of the compressional data.

Figure 9. (a) Cr^{3+} R-line splitting (R_1-R_2) of δ-AlOOH as a function of pressure. The inset shows the quadratic elongation (QE) values at high pressure. (b) The AlO_6 octahedron in $P2_1nm$-phase δ-AlOOH. (c) The AlO_6 octahedron in *Pnnm*-phase δ-AlOOH. The large silver, medium-red and small white spheres represent Al, O and H atoms, respectively.

This is the peer-reviewed, final accepted version for American Mineralogist, published by the Mineralogical Society of America.
The published version is subject to change. Cite as Authors (Year) Title. American Mineralogist, in press.
DOI: https://doi.org/10.2138/am-2022-8005. http://www.minsocam.org/

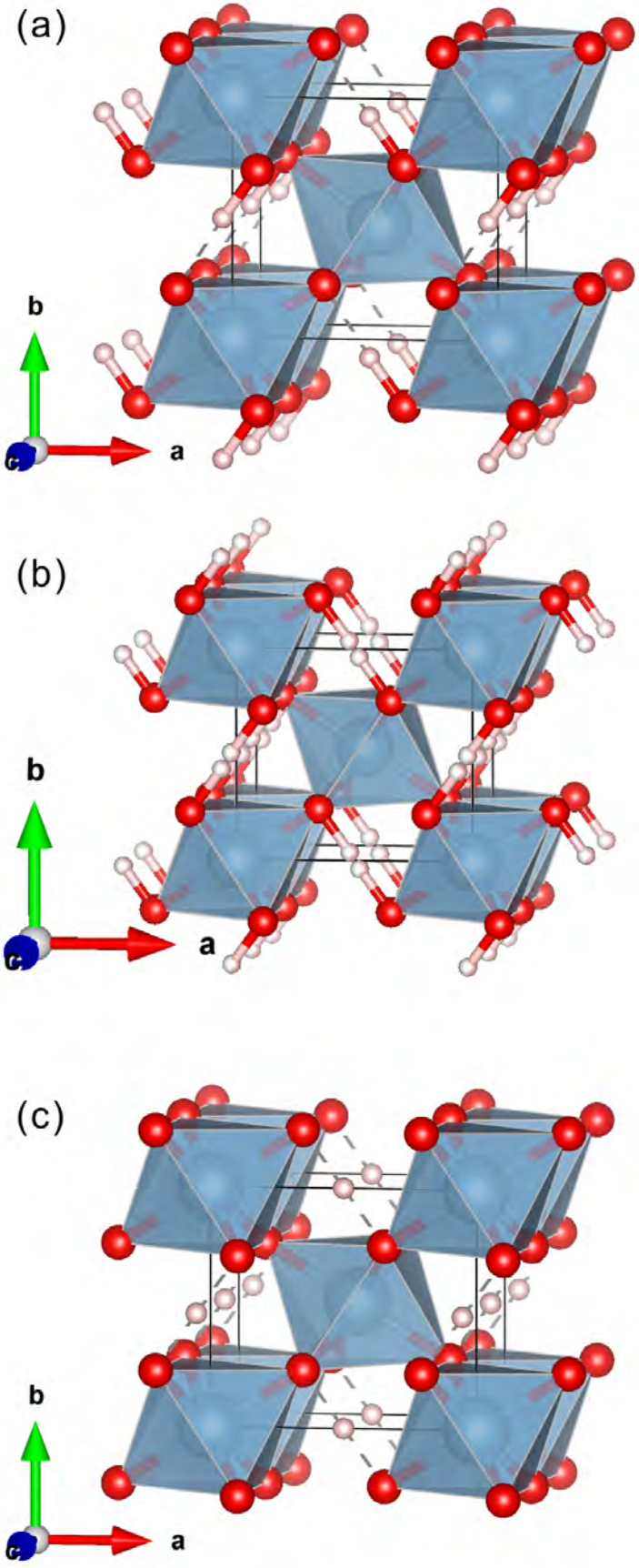

Figure1

This is the peer-reviewed, final accepted version for American Mineralogist, published by the Mineralogical Society of America.
The published version is subject to change. Cite as Authors (Year) Title. American Mineralogist, in press.
DOI: https://doi.org/10.2138/am-2022-8005. http://www.minsocam.org/

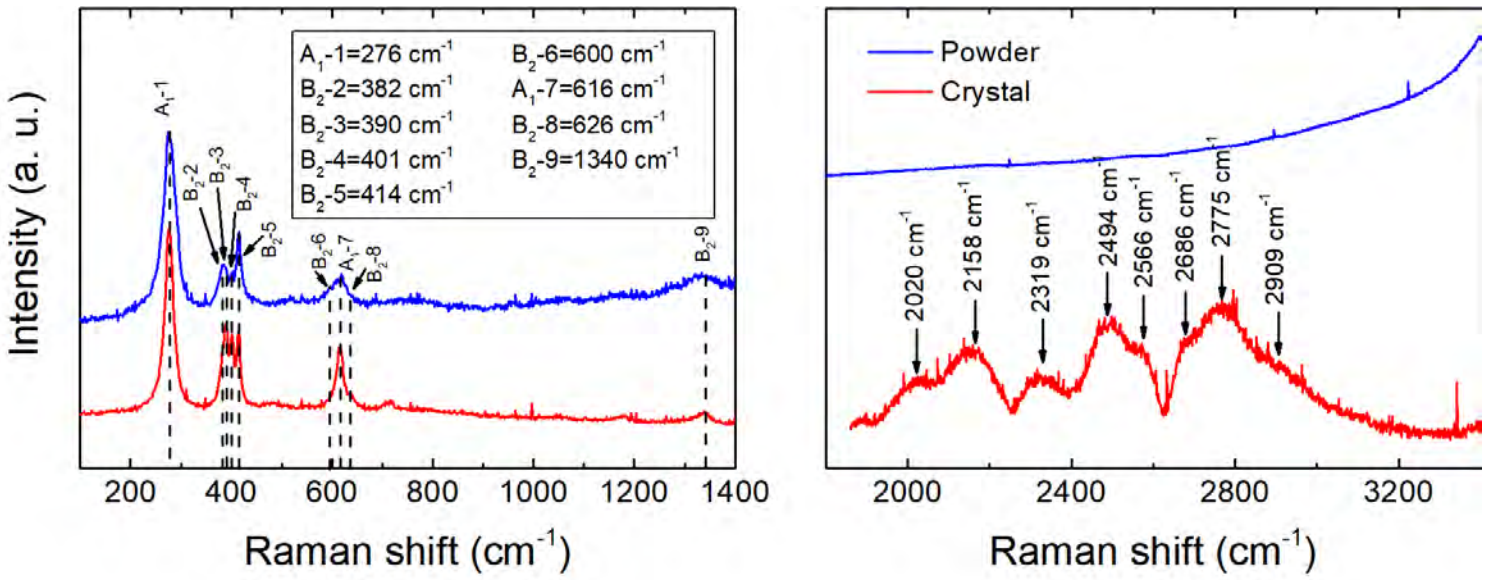

Figure2

This is the peer-reviewed, final accepted version for American Mineralogist, published by the Mineralogical Society of America.
The published version is subject to change. Cite as Authors (Year) Title. American Mineralogist, in press.
DOI: https://doi.org/10.2138/am-2022-8005. http://www.minsocam.org/

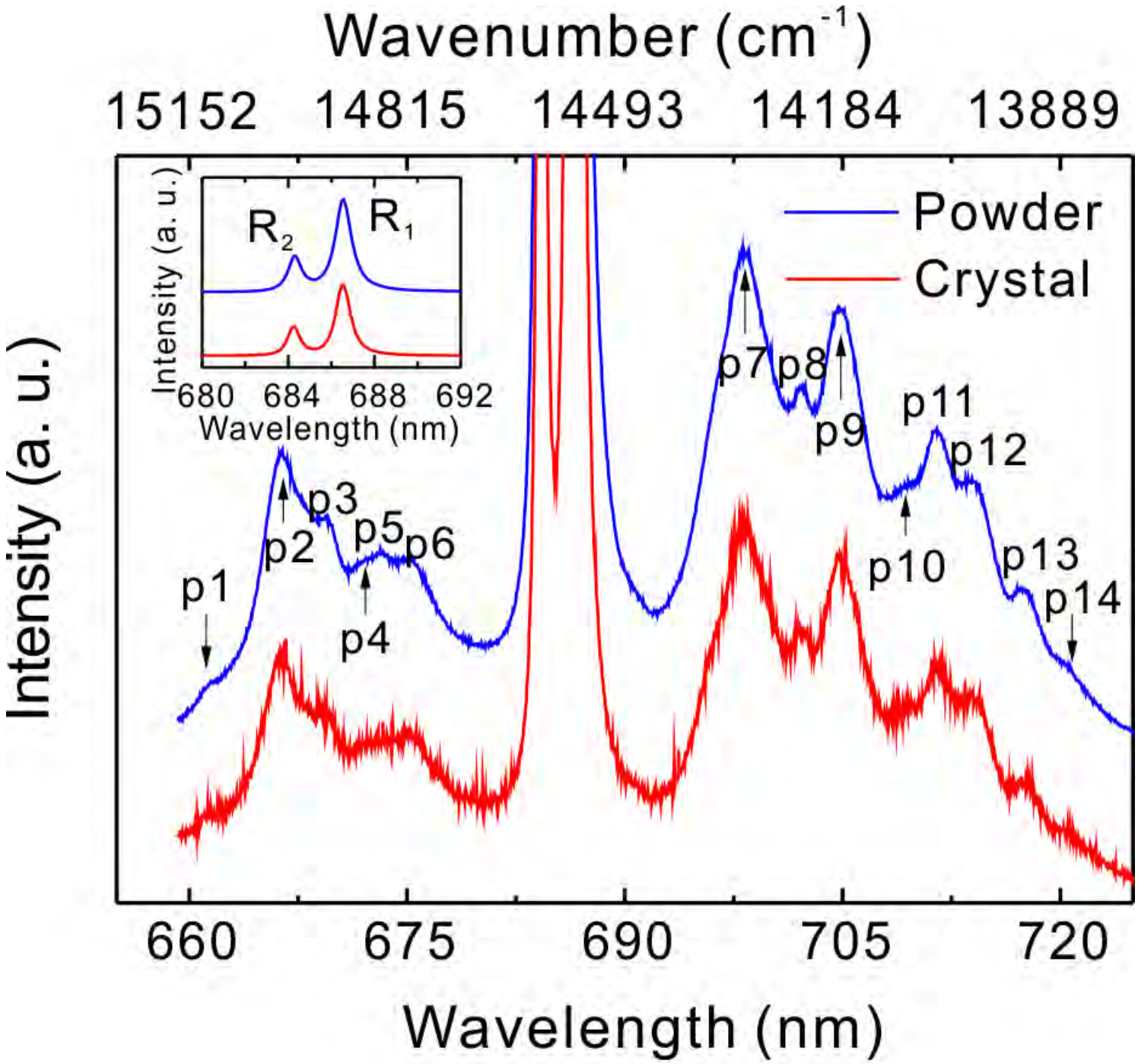

Figure3

This is the peer-reviewed, final accepted version for American Mineralogist, published by the Mineralogical Society of America.
The published version is subject to change. Cite as Authors (Year) Title. American Mineralogist, in press.
DOI: https://doi.org/10.2138/am-2022-8005. http://www.minsocam.org/

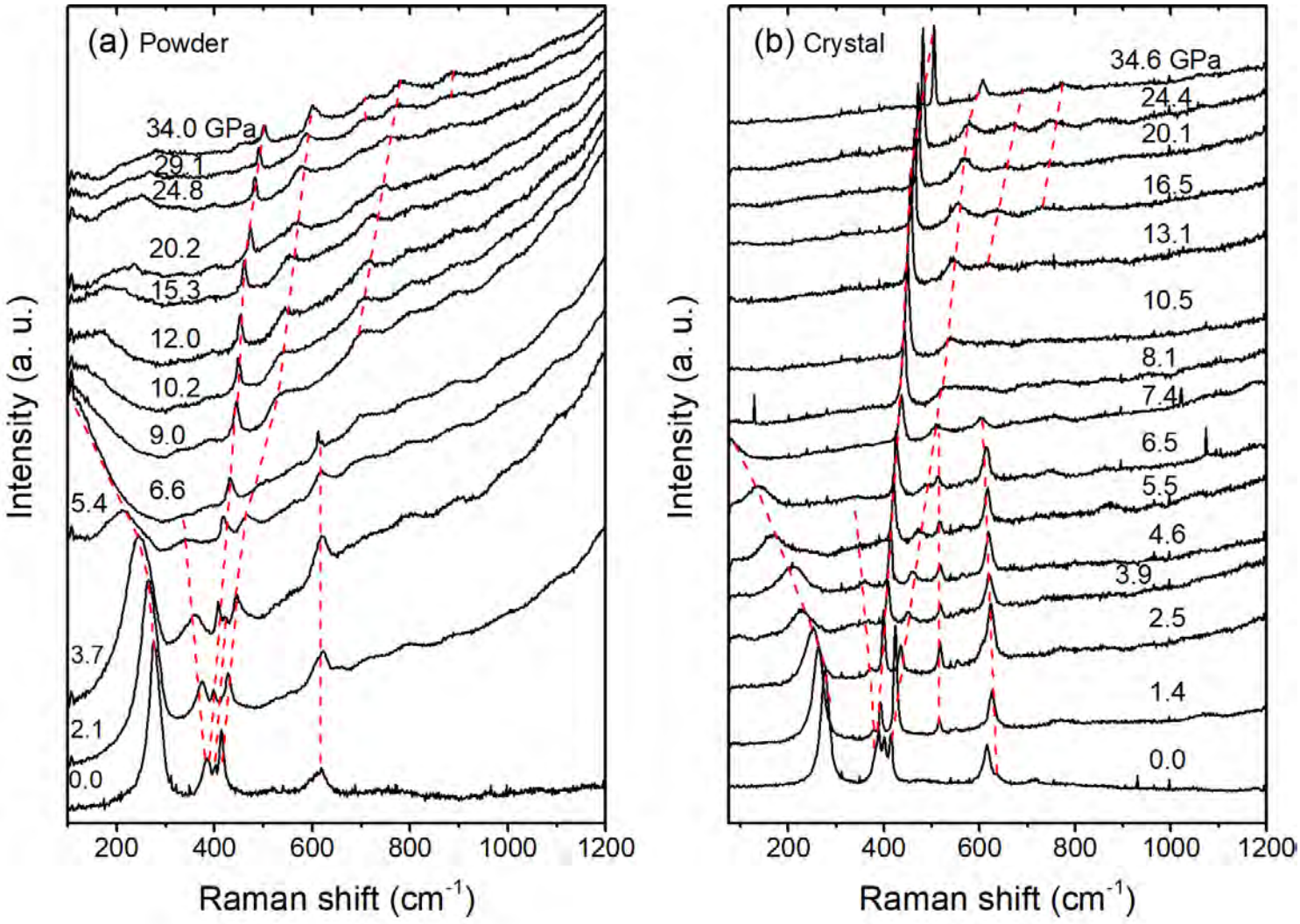

Figure4

This is the peer-reviewed, final accepted version for American Mineralogist, published by the Mineralogical Society of America.
The published version is subject to change. Cite as Authors (Year) Title. American Mineralogist, in press.
DOI: https://doi.org/10.2138/am-2022-8005. http://www.minsocam.org/

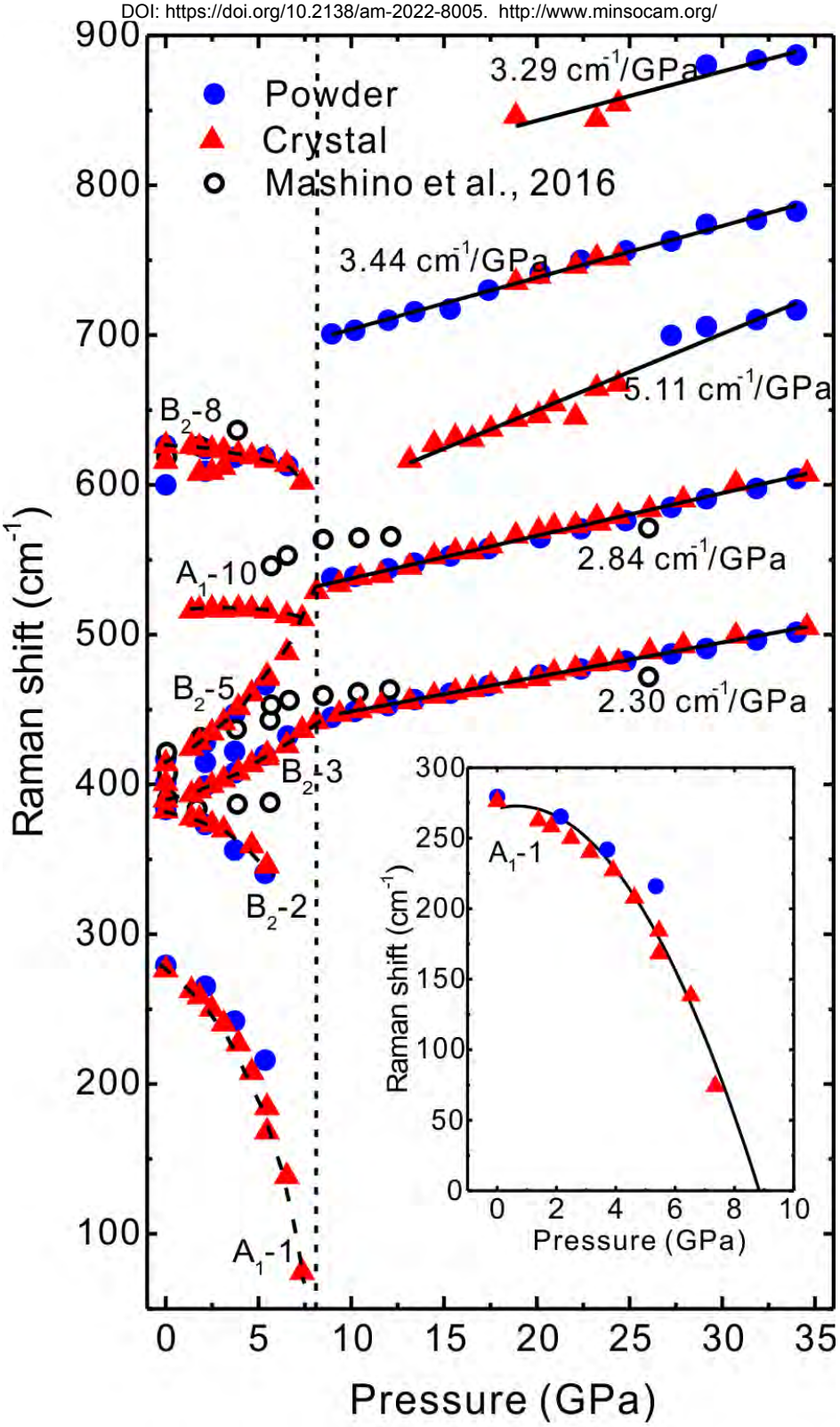

Figure5

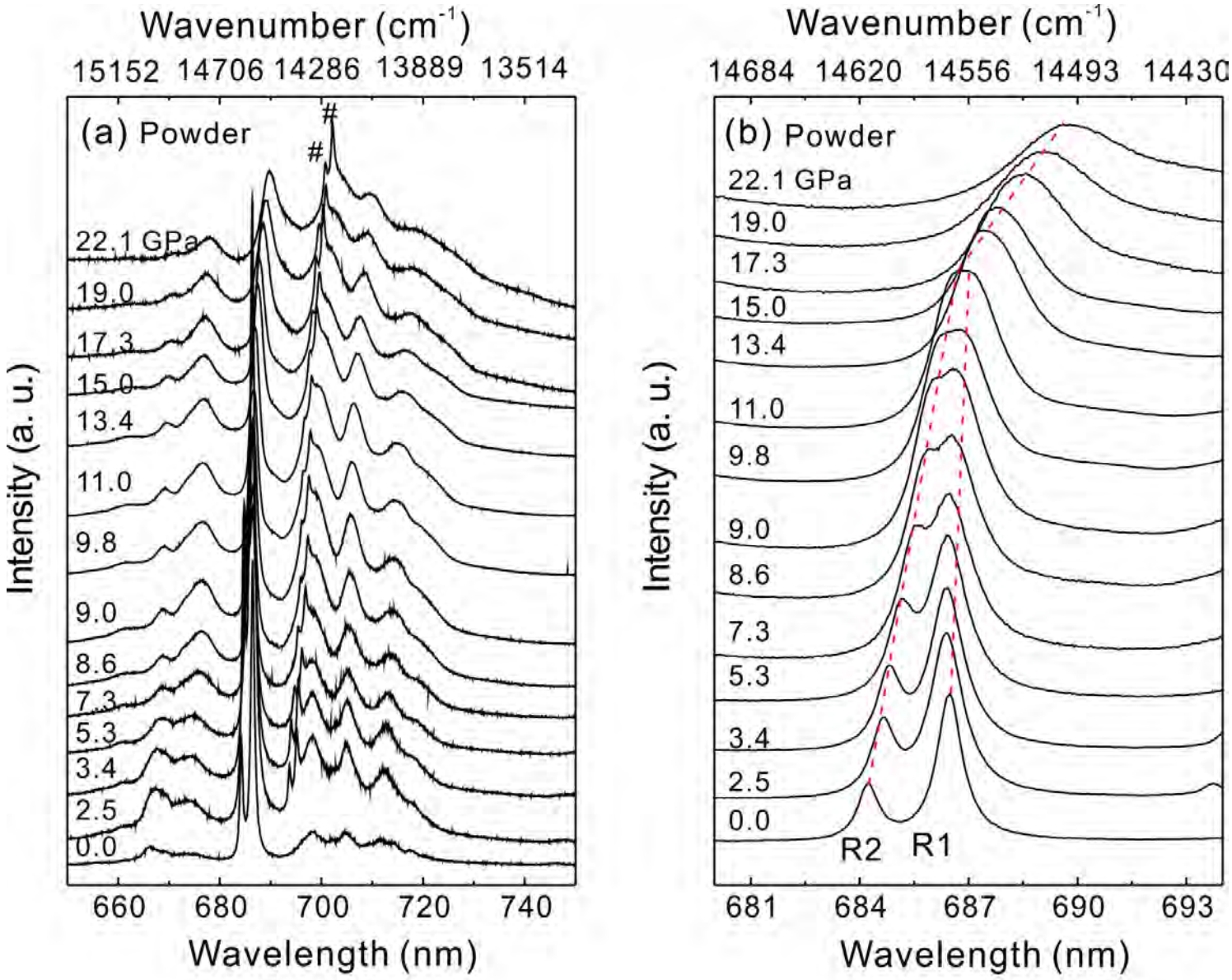

Figure6

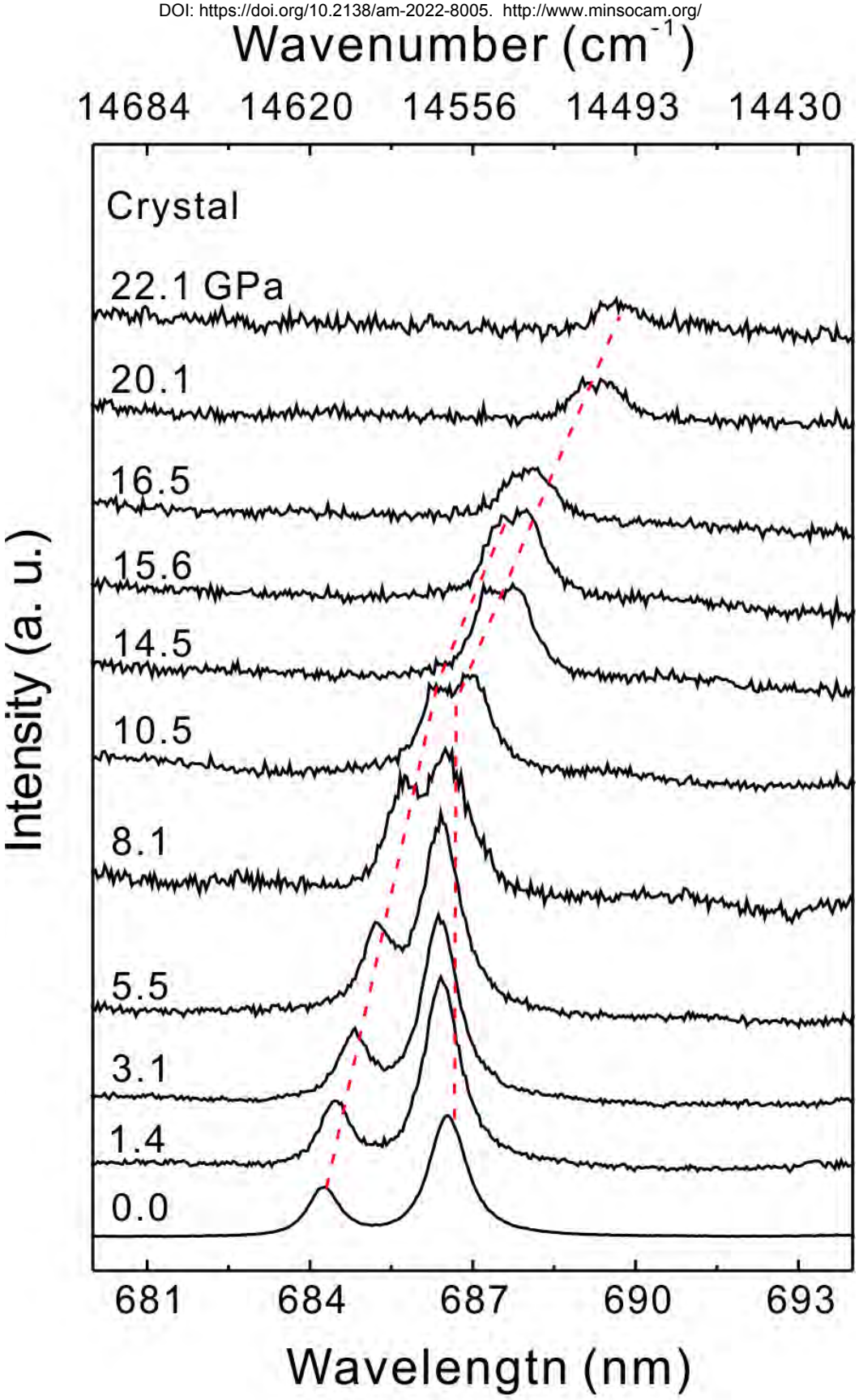

Figure7

This is the peer-reviewed, final accepted version for American Mineralogist, published by the Mineralogical Society of America.
The published version is subject to change. Cite as Authors (Year) Title. American Mineralogist, in press.
DOI: https://doi.org/10.2138/am-2022-8005. http://www.minsocam.org/

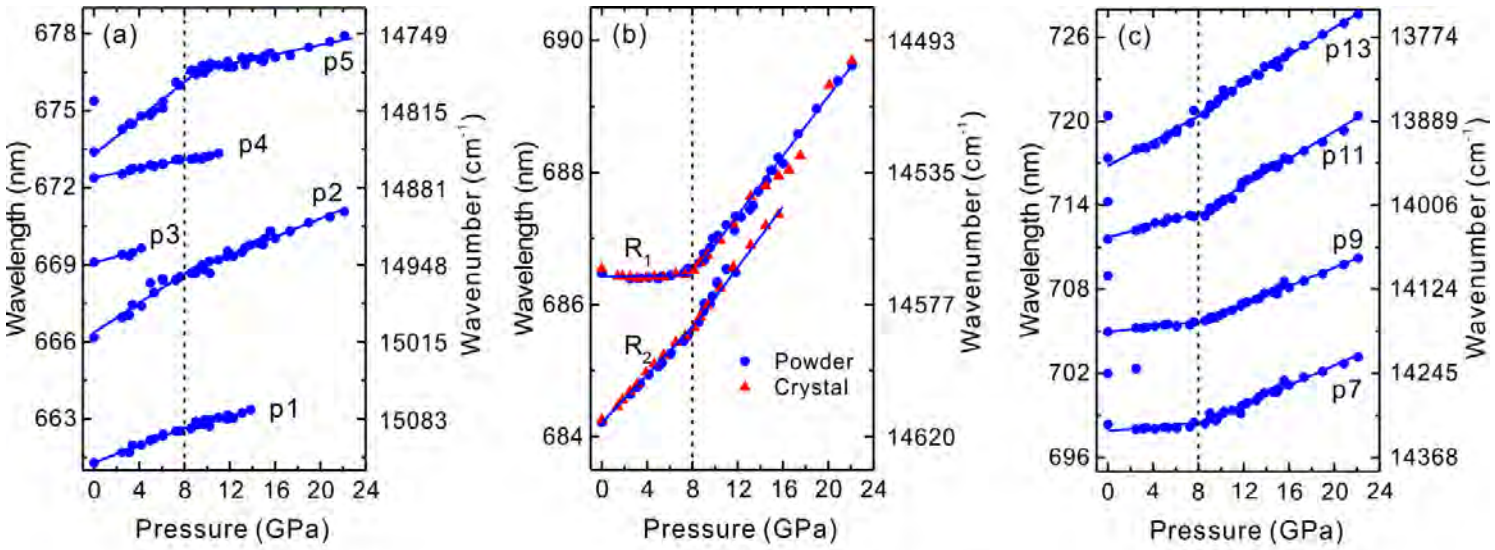

Figure8

This is the peer-reviewed, final accepted version for American Mineralogist, published by the Mineralogical Society of America.
The published version is subject to change. Cite as Authors (Year) Title. American Mineralogist, in press.
DOI: https://doi.org/10.2138/am-2022-8005. http://www.minsocam.org/

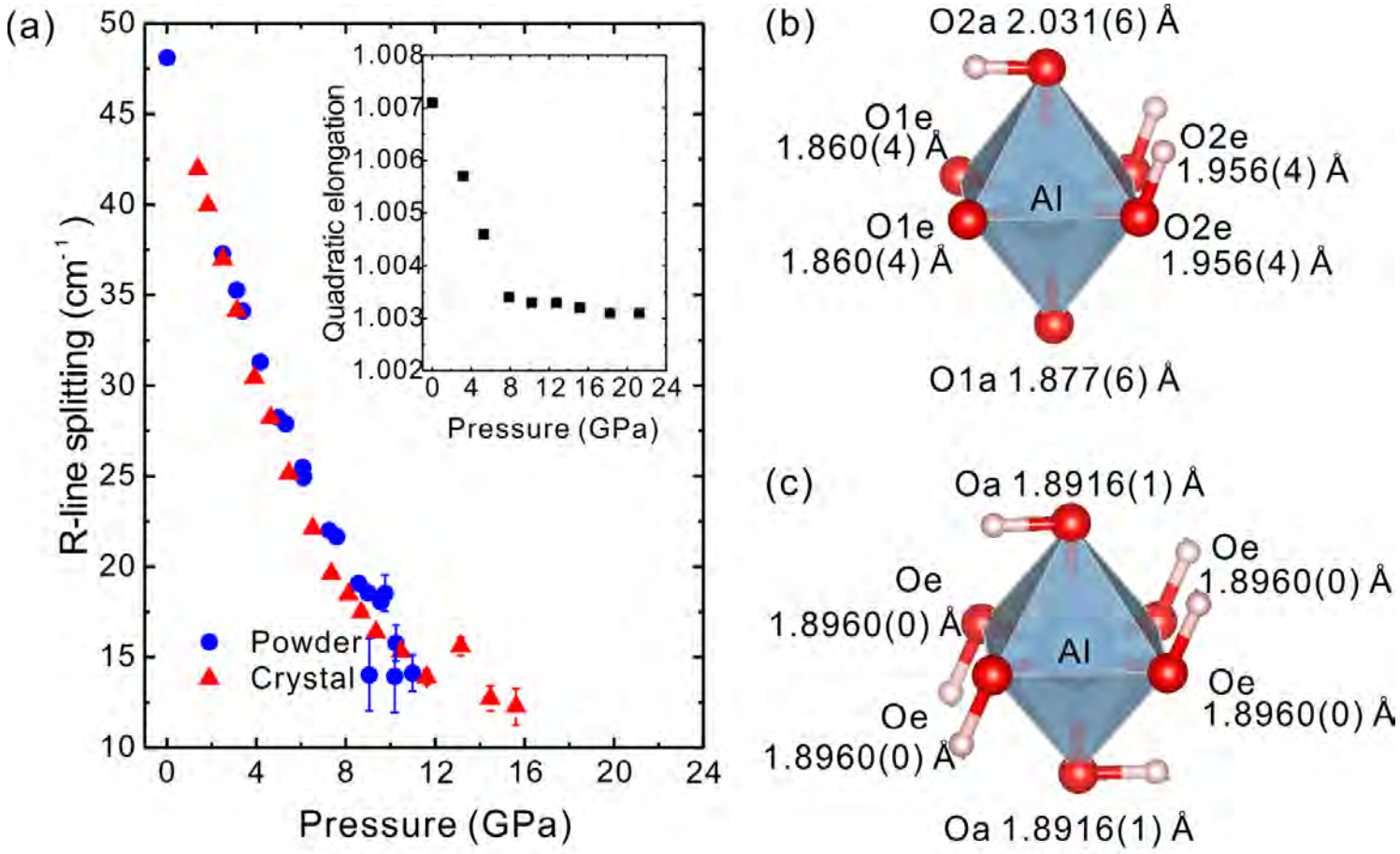

Figure9